RESEARCH ARTICLE

SusMat WILEY

Rapid preparation of carbon-supported ruthenium nanoparticles by magnetic induction heating for efficient hydrogen evolution reaction in both acidic and alkaline media

Qiming Liu[1] | Bingzhang Lu[1] | Forrest Nichols[1] | Jeffrey Ko[2] | Rene Mercado[1] | Frank Bridges[2] | Shaowei Chen[1]

[1]Department of Chemistry and Biochemistry, University of California, Santa Cruz, California, USA

[2]Department of Physics, University of California, Santa Cruz, California, USA

Correspondence
Shaowei Chen, Department of Chemistry and Biochemistry, University of California, Santa Cruz, California 95064, United States.
Email: shaowei@ucsc.edu

Qiming Liu and Bingzhang Lu contributed equally to this work.

Abstract

Ruthenium has been hailed as a competitive alternative for platinum toward hydrogen evolution reaction (HER), a critical process in electrochemical water splitting. In this study, we successfully prepare metallic Ru nanoparticles supported on carbon paper by utilizing a novel magnetic induction heating (MIH) method. The samples are obtained within seconds, featuring a Cl-enriched surface that is unattainable via conventional thermal annealing. The best sample within the series shows a remarkable HER activity in both acidic and alkaline media with an overpotential of only -23 and -12 mV to reach the current density of 10 mA/cm^2, highly comparable to that of the Pt/C benchmark. Theoretical studies based on density functional theory show that the excellent electrocatalytic activity is accounted by the surface metal-Cl species that facilitate charge transfer and downshift the d-band center. Results from this study highlight the unique advantages of MIH in rapid sample preparation, where residual anion ligands play a critical role in manipulating the electronic properties of the metal surfaces and the eventual electrocatalytic activity.

KEYWORDS
Cl-enriched surface, density functional theory, hydrogen evolution reaction, magnetic induction heating, ruthenium

1 | INTRODUCTION

With the ever-increasing need of energy and the rapid depletion of traditional fossil fuels, hydrogen gas (H$_2$) has been considered as one of the most promising green energy resources. However, currently H$_2$ is produced mostly by steam-methane reforming at high temperatures (700–1000°C), making it energy- and capital-consuming.[1] Electrochemical water splitting (water electrolyzer) represents an effective alternative, where H$_2$ is produced at

the cathode using electricity produced from a sustainable source such as wind, sun light, and hydraulics. Yet, an appropriate catalyst is needed to catalyze the hydrogen evolution reaction (HER) so as to decrease the overpotential and increase the current density. Thus far, Pt-based nanoparticles have remained the catalysts of choice toward HER; yet the high cost and limited natural abundance have hampered the wide-spread applications.[2,3]

Ruthenium (Ru), which costs about half of Pt, has emerged as a viable substitute, due to its similar bonding strength with hydrogen (∼65 kcal/mol) to that of Pt-H, a critical parameter in dictating the HER activity.[4] Nevertheless, in the well-known volcano plot of the hydrogen adsorption Gibbs-free energy (ΔG_{H*}),[5,6] Ru is actually situated on the left side, suggesting a somewhat strong adsorption of H that is unfavorable for H desorption from the catalyst surface. Computational studies based on density functional theory (DFT) have shown that H adsorption onto the top sites of Ru(0001) facet possesses an almost ideal ΔG_{H*} of only −0.07 eV, in comparison to the adjacent hollow Ru_3 sites that exhibit a far more negative ΔG_{H*} of ca. −0.45 eV, suggesting that the latter is actually the most likely dominant binding sites, leading to a nonideal HER performance.[7] In another study, Li et al.[8] investigated the effect of ruthenium crystallinity on the HER activity and observed that the ΔG_{H*} on the hollow or bridge sites on most facets of *hcp* Ru and *fcc* Ru ranged from −0.5 to −0.7 eV, markedly greater than that on Pt(111) (ca. 0 eV).[9] This indicates that manipulation of the Ru crystallinity alone is unlikely to be effective in diminishing ΔG_{H*} for optimal HER.

The preparation of nanocomposite catalysts with Ru supported on select functional substrates (i.e., carbon, nitride, oxide, etc.) has been adopted as a feasible strategy to tune the energetics of H adsorption.[10] For instance, Ru nanoparticles supported on graphitic carbon nitride (g-C_3N_4) outperformed Pt in alkaline HER, due to the reduced energy barrier of water dissociation and optimal ΔG_{H*}.[7] Ru atomically dispersed into g-C_3N_4 or N-doped carbon also showed unprecedented HER performance in both alkaline and acidic media, owning to the unique Ru-N/C atomic coordination for optimal adsorption of H.[11–13] Alloying is another strategy to control the electronic structure of Ru. For example, Cai et al.[14] synthesized ultrathin RuCo alloy nanosheets and observed a low overpotential (η_{10}) of −10 mV to reach the current density of 10 mA/cm^2 in 1 M KOH, consistent with results from DFT studies that Ni or Co could efficiently downshift the d-band center of Ru and weaken H* adsorption. Nonmetal elements have also been integrated into Ru producing RuX hybrids (X = B, Si, P, S, Se, and Te) to tune the electronic structure and the adsorption of H* on Ru.[7,15–19] For instance, interstitial alloying of Si atoms into Ru has been found to render the top adsorption of H* to be dominant, leading to an HER activity that rivals that of commercial Pt.[7] In addition, it has been shown that the surface electronic structure of Ru can be manipulated by coordination with P atoms, where electron transfer from Ru to P dopants reduced ΔG_{H*} and, hence, enhanced activities towards both HER and HOR (hydrogen oxidation reaction).[20]

In these prior studies, the Ru-based catalysts were typically prepared by wet chemical reduction or pyrolysis, and a range of chemicals and solvents are consumed, making the process nonsustainable and time consuming. In the present study, we report a novel method based on magnetic induction heating (MIH) to synthesize Ru nanoparticles supported on carbon paper within seconds. Notably, in the ultrafast heating-quench process, metallic Ru nanoparticles were generated and deposited evenly on carbon paper by thermal decomposition of $RuCl_3$ salt even in the ambient atmosphere. Because of the short heating duration, $RuCl_3$ was incompletely decomposed, leading to residual Cl on the Ru surface with the content readily controlled by the magnetic current and heating time. This turned out to play a critical role in the HER performance of the samples, as confirmed in DFT studies, where the surface Cl species influenced the electronic structure of metallic Ru and the adsorption configuration and energetics of H*. Among the series, the best sample was obtained with a magnetic current of 300 A and heating time of 6 s, which demonstrated an HER activity similar to that of commercial Pt/C in both alkaline and acidic media with a respective η_{10} of −12 and −23 mV.

2 | RESULTS AND DISCUSSION

2.1 | Sample preparation

The synthesis of Ru nanoparticles supported on carbon paper consisted of two major steps, as shown in Figure 1A. A $RuCl_3$ solution was first dropcast onto a piece of pretreated carbon paper and dried at room temperature for 10 min. The carbon paper was then wrapped with graphite paper and sandwiched between two iron sheets, and the assembly was placed into the middle of the induction coil of a magnetic induction heater and heated at a controlled current for a varied period of time before being dropped into a beaker containing cold ethanol (−78°C) to quench the sample and to prevent oxidation in air (Figure 1B). By virtue of the Joule effect, the iron sheets can be heated up to ca. 1500°C at an ultrafast rate (up to 200 K/s^1, Figure 1C) due to the Eddy current generated instantly by the magnetic field. As a thermal-radiative material, carbon paper can be heated up simultaneously, converting $RuCl_3$ into Ru nanoparticles supported on carbon paper.
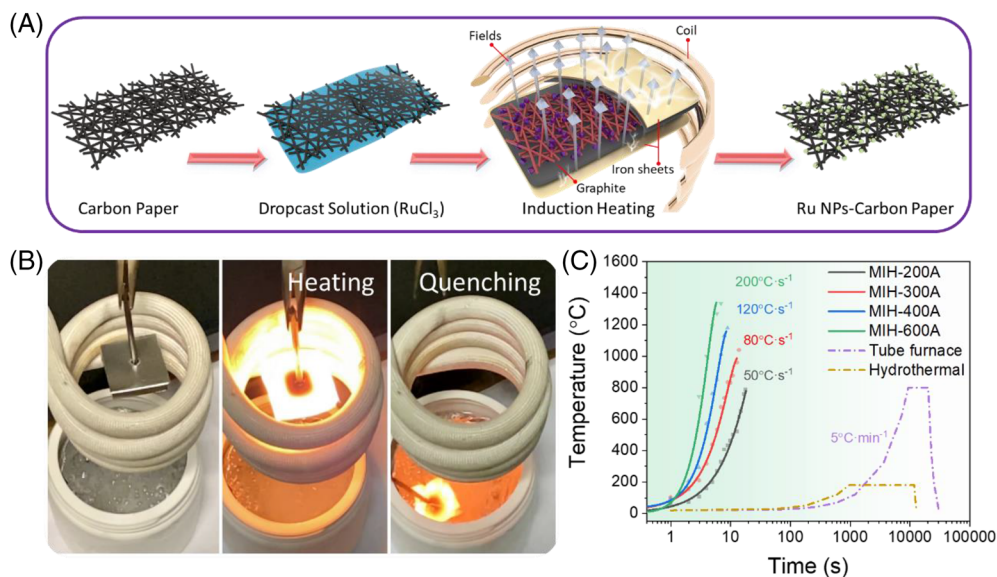
FIGURE 1 (A) Schematic illustration of the preparation of Ru nanoparticles supported on carbon paper by magnetic induction heating. (B) Photographs of the synthetic process. (C) Heating temperature as the function of time by using MIH at different heating currents, as determined with an infrared thermometer (Supporting information Figure S1)

2.2 | Structural characterizations

The structure of the samples was first characterized by transmission electron microscopy (TEM) measurements. From Figure 2 and Supporting information Figures S2-S4, one can clearly see a structural evolution of the ruthenium species from an amorphous state to metallic ruthenium nanoparticles with increasing magnetic current. For instance, for Ru-200 that was prepared by MIH treatment at 200 A for 6 s, the sample contained mostly amorphous particles (2–5 nm in diameter), as manifested in bright-field TEM measurements (Supporting information Figure S2). This was likely because the temperature was not sufficiently high for the complete decomposition of $RuCl_3$ and for the production of crystalline nanoparticles. When the magnetic current was increased to 300 A, the corresponding sample, Ru-300 (Figure 2A), actually consisted of nanoparticles evenly distributed on the carbon paper, most of which fell in the size range of 2 to 10 nm in diameter (Figure 2B), with an average size of 6 nm. Additionally, clearly defined lattice fringes can be resolved from these nanoparticles in high-resolution TEM measurements (Figure 2C), featuring two interplanar spacings of ca. 0.135 and 0.205 nm that can be ascribed to hcp Ru(11-20) and (10-11) facets (JCPDS-ICDD card No. 06–0663), respectively. The good crystallinity of the nanoparticle can also be evidenced in the bright spots of the fast Fourier transform of the TEM image, as shown in the insets of Figure 2C and Supporting information Figure S3, suggesting the formation of *hcp* Ru nanoparticles. At even higher magnetic currents (e.g., Ru-600, Supporting information Figure S4),

apparent aggregation of crystalline Ru occurred forming large agglomerates.

The sample morphology can also be readily manipulated by the heating time. For instance, when the heating time was reduced to 3 s (Ru-300-S), only amorphous particles were produced on carbon (Supporting information Figure S5); yet with the heating time prolonged to 12 s (Ru-300-L), the sample consisted mostly of *hcp* Ru agglomerates (Supporting information Figure S6). Taken together, these results suggest that 300 A and 6 s represent the optimal conditions to produce *hcp* Ru nanoparticles that were well dispersed on the surface of carbon paper, a unique feature conducive for HER electrocatalysis (vide infra).

Indeed, elemental mapping analysis based on electron energy loss spectroscopy (EELS) measurements showed that Ru was mostly confined within the nanoparticles, along with residual O and Cl (Figure 2D). These elements can also be identified in X-ray photoelectron spectroscopy (XPS) measurements. From the XPS survey spectra in Supporting information Figure S7, the Ru 3d, C 1s, Ru 3p, and O 1s peaks can be clearly resolved at ca. 280, 284, 474, and 530 eV, respectively, in all samples. Notably, the Cl 2p peak (ca. 200 eV) can also be seen in some of the samples that were prepared at relatively low currents for a short heating time, such as Ru-200, Ru-300 and Ru-300-S, suggesting the formation of residual Cl. By sharp contrast, the Cl 2p peak vanished in samples prepared by prolonged heating at a higher current, such as Ru-400, Ru-600, and Ru-300-L, implying complete decomposition of $RuCl_3$ into Ru nanoparticles.
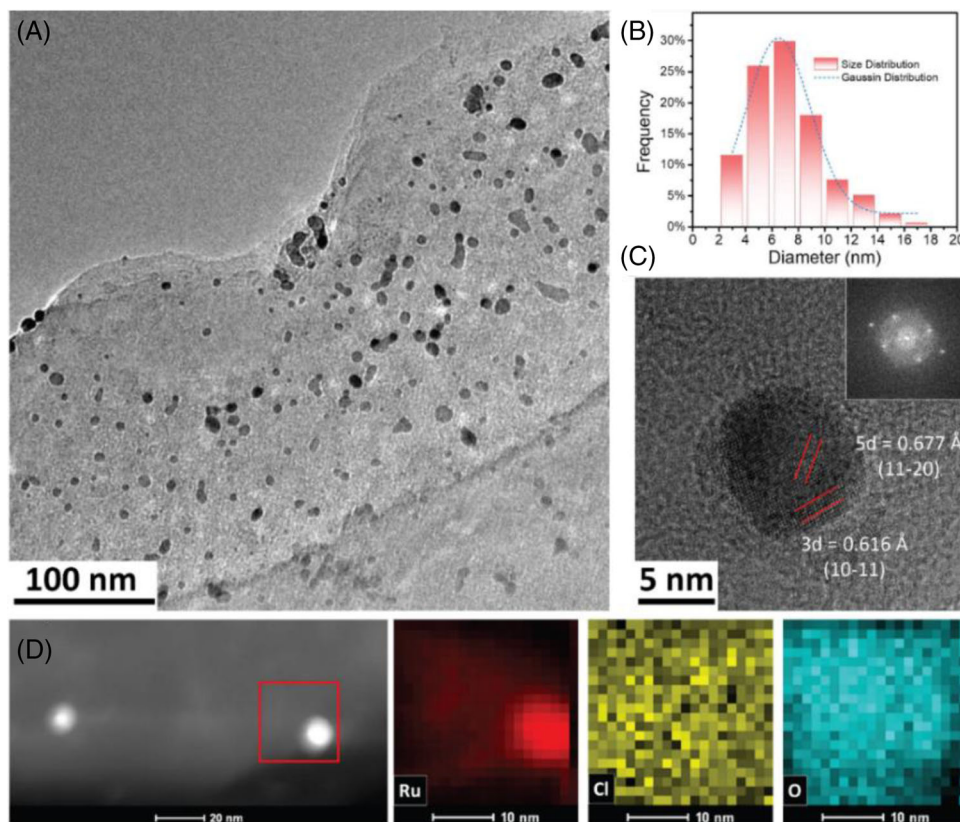
FIGURE 2 TEM studies of the Ru-300 sample. (A) TEM image of Ru nanoparticles at low magnification and (B) the corresponding core size histogram. (C) HRTEM image of a Ru nanoparticle with the corresponding fast-Fourier transform (FFT) image shown in the inset. (D) ADF-TEM image of Ru nanoparticles and the corresponding elemental maps of the red-circled area

Figure 3A shows the high-resolution scans of the Ru 3p electrons in the series of samples prepared at different magnetic currents (200 to 600 A) but for the same heating time of 6 s. One can see that the Ru-600 sample consisted of a single doublet (red peaks) at 461.1/483.3 eV arising from the $3p_{3/2}/3p_{1/2}$ electrons of metallic ruthenium,[21–23] consistent with results from TEM measurements where large agglomerates of crystalline Ru were found (Supporting information Figure S4). For Ru-400 that was prepared at a lower magnetic current, in addition to the metallic Ru $3p_{3/2}/3p_{1/2}$ pair at 461.2/483.4 eV, a small, second doublet (blue peaks) can be resolved at 463.9/485.1 eV, signifying the formation of electron-deficient Ru likely in the forms of $RuCl_x/RuO_y$ species.[21,24–26] The latter became more pronounced in Ru-300 (464.1/486.3 eV), with the corresponding metallic peaks at 461.6/483.8 eV. Ru-200 exhibited an even more prominent doublet for the $RuCl_x/RuO_y$ species, though at a binding energy of about 0.8 eV higher at 465.3/487.5 eV. The other doublet (orange peaks) can be deconvoluted at 462.7/484.9 eV, which were at least 1.1 eV higher than those of the other samples in the series but markedly lower than those of $RuCl_3$ (464.1 eV for Ru $3p_{3/2}$),[21] suggesting only partial decomposition of $RuCl_3$ and the formation of amorphous Ru nanoclusters as observed in TEM measurements

(Supporting information Figure S2). In fact, on the basis of the integrated peak areas, one can see a clear decline of the relative content of the $RuCl_x/RuO_y$ species in total Ru with increasing magnetic current, Ru-200 (49.7%) > Ru-300 (29.3%) > Ru-400 (11.5%) > Ru-600 (0%) (Supporting information Tables S1).[8,27]

A similar trend was observed when the heating duration was increased at a fixed magnetic current. From Supporting information Figure S8, one can see that the binding energies of the Ru $3p_{3/2}/3p_{1/2}$ peaks decreased by ca. 1.3 eV from Ru-300-S to Ru-300 and Ru-300-L, and the fraction of the $RuCl_x/RuO_x$ species diminished accordingly, Ru-300-S (45.5%) > Ru-300 (29.3%) > Ru-300-L (17.8%). It should be noted that in comparison with Ru-200, the Ru $3p_{3/2}/3p_{1/2}$ binding energies of Ru-300-S were ca. 0.3 eV higher, implying an even lower degree of decomposition of $RuCl_3$ into Ru nanoparticles. That is, prolonged heating facilitates the formation of metallic Ru nanoparticles, consistent with the TEM results (Figure 2 and Supporting information Figures S2-S6). The corresponding Ru 3d profiles are also in good agreement (Supporting information Figure S9).

Consistent results were obtained from the Cl 2p spectra. From Figure 3B, one can clearly see that Ru-200,
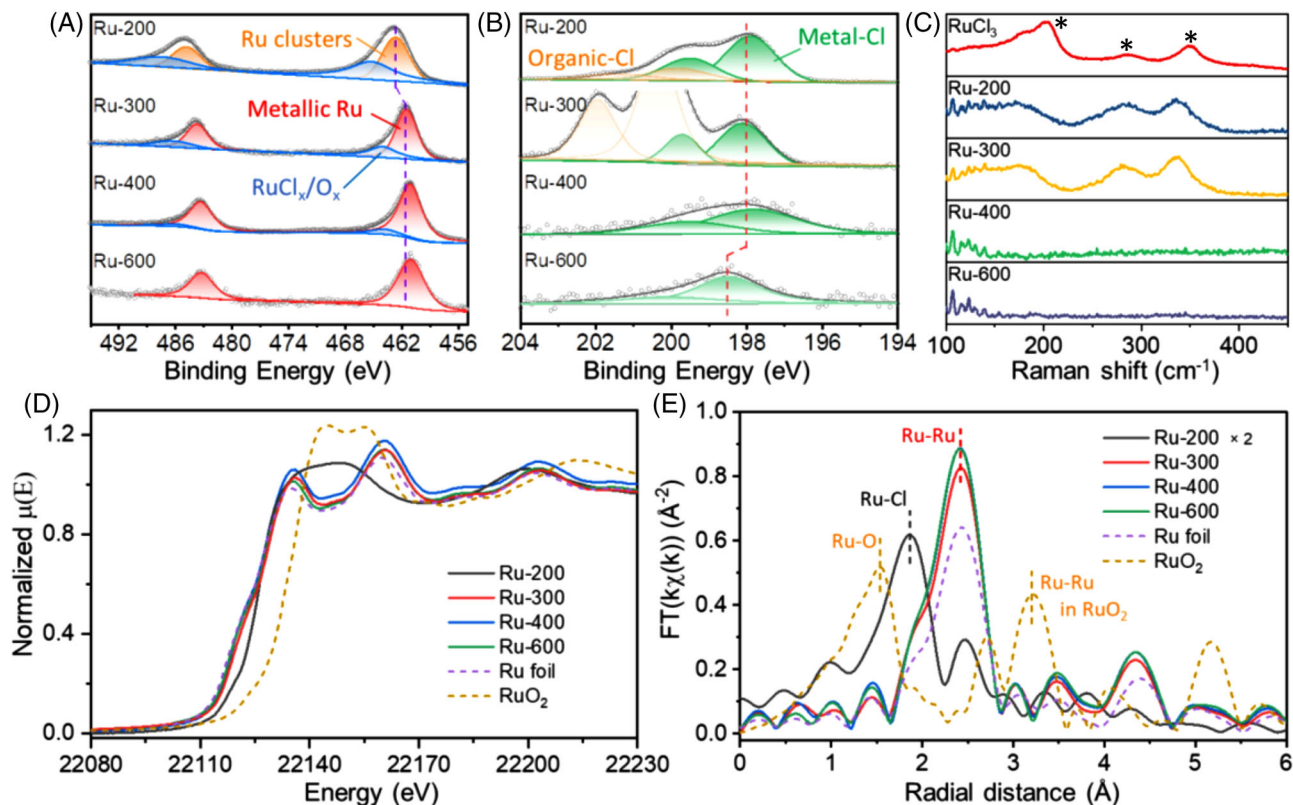
FIGURE 3 (A) Ru 3p XPS spectra and (B) Cl 2p XPS spectra of Ru-200, Ru-300, Ru-400, and Ru-600. (C) Raman spectra of $RuCl_3$, Ru-200, Ru-300, Ru-400, and Ru-600. (D) X-ray absorption near-edge spectra (XANES), and (E) the corresponding Fourier transformed extended X-ray absorption spectra (FT-EXAFS) of Ru-200, Ru-300, Ru-400, and Ru-600. "Ru-Ru" in red represents Ru-Ru bonds in metallic Ru, while "Ru-Ru" in orange represents Ru-Ru bonds in RuO_2

Ru-300, and Ru-400 all possessed a doublet (green peaks) at 198.0/199.6 eV that can be assigned to Ru-Cl_x.[24,28,29] For Ru-600, this doublet appears at a higher binding energy by (ca. 0.5 eV) suggesting weakened interaction between Cl and Ru, likely because of structural hinderance by a thin carbon shell, as observed in TEM measurements (Supporting information Figure S4C). For Ru-200 and Ru-300, a second doublet emerged at 200.0/201.6 eV that can be ascribed to organic Cl (orange peaks, C-Cl_x or O-Cl_x species),[28] which vanished altogether in Ru-400 and Ru-600, implying thermal instability of the organic Cl species. Furthermore, the content of Ru-Cl_x diminished appreciably with increasing magnetic current (Supporting information Table S1),[24] Ru-200 (6.24 at%) > Ru-300 (0.96 at%) > Ru-600 (0.47 at%) > Ru-400 (0.35 at%). This suggests almost complete decomposition of $RuCl_3$ into Ru nanoparticles at a current greater than 400 A for a heating time of at least 6 s. A similar trend was observed when the magnetic current was fixed at 300 A, with the heating time increased from 3 s (Ru-300-S) to 12 s (Ru-300-L), which led to a clear diminishment of the organic Cl species, and Ru-Cl_x being the increasingly dominant component in the sample (Supporting information Figure S10).

The C 1s and O 1s spectra of the samples series also provide important insights into the structural change during the ultrafast heating process. One can see from Supporting information Figure S9 that with increased magnetic current, the main C 1s peak decreased from ca. 284.4 eV for Ru-200 and Ru-300 to ca. 284.1 eV for Ru-400 and Ru-600, implying that the carbon substrate was somewhat electron-deficient at low currents. As for the O 1s spectra (Support information Figure S11A), the major species were C-O (533.5 eV) and C=O (531.5 eV) moieties on carbon paper. With increasing magnetic current (temperature), the C=O peaks diminished in intensity, and the overall O content decreased from 14.5 at% for Ru-200 to ca. 7% for other samples prepared at higher magnetic currents (Supporting information Table S1). It is likely that the decomposition of these oxygen groups produced CO and/or CO_2,[30] facilitating the carbothermal reduction of RuCl_x to ruthenium nanoparticles and protection against oxidation. Yet, with a prolonged heating duration, the overall content of O increased from 7.3 at% for Ru-300 to 11.3 at% for Ru-300-L (Supporting information Figure S11B). Notably, for Ru-200, Ru-300, and Ru-400, there is a minor peak at 530.0 eV suggesting the formation of RuO_x species on the nanoparticle

surface (it is unlikely to be bulk RuO_2 as no RuO_2 lattice fringes were observed in TEM measurements).

Taken together, these results suggest the successful transformation of $RuCl_3$ into Ru nanoparticles by MIH, which were decorated with $RuCl_x/RuO_y$ species on the surface.

Raman spectroscopic measurements showed that abundant $RuCl_x$ species were indeed formed in Ru-200 and Ru-300, but not in Ru-400 or Ru-600. From Figure 3C, one can see that $RuCl_3$ (on carbon paper) exhibited three major peaks at 202, 286, and 350 cm^{-1} (marked with asterisks), which can be assigned to the different A_g vibrational modes of Ru-Cl.[31–33] Notably, these three bands red-shifted somewhat for Ru-200 and Ru-300 to 171, 280, and 336 cm^{-1}, respectively. This may be accounted for by the change of the stacking mode and symmetry of the Ru-Cl species in comparison to pristine $RuCl_3$,[32] as a result of the decomposition of $RuCl_3$ during the ultrafast heating process. No apparent signals of Ru-Cl could be discerned from the spectra of Ru-400 or Ru-600, consistent with the complete decomposition of $RuCl_x$ into metallic Ru in these samples, as manifested in XPS measurements.

Further structural details of the samples were obtained from X-ray absorption spectroscopy (XAS) measurements. Figure 3D shows the X-ray absorption near-edge spectra (XANES) of the Ru K edge of the sample series. One can see that the absorption edge of Ru-200 was situated between those of Ru foil and RuO_2, suggesting an average valence state between 0 and +4, consistent with the incomplete decomposition of $RuCl_3$ into Ru nanoparticles, as suggested in the above XPS measurements (Figure 3A). For other samples prepared at higher magnetic currents, the absorption edges, as well as the postedge modulations, were all almost identical to those of Ru foil, confirming that metallic Ru was the dominant species in these samples, in excellent agreement with the TEM and XPS results (Figures 2 and 3). This also implies that the $RuO_x/RuCl_y$ species represent only a trace amount and were mostly residing only on the surface of Ru nanoparticles.

The corresponding Fourier-transformed extended X-ray absorption fine structure (FT-EXAFS) spectra are depicted in Figure 3E. One can see that Ru-200 exhibits a main peak at 1.86 Å, most likely arising from the Ru-Cl path,[26,29] and another at 2.48 Å due to the Ru-Ru bond,[13] which is slightly greater than that of Ru foil (2.42 Å). Fitting of the EXAFS data was then performed for the six samples in the series. Ru-200 is fitted by using a hexagonal $RuCl_3$ and hexagonal metallic Ru structure with a dummy variable incorporated to model the fraction of $RuCl_3$ to metallic Ru within the sample. The remaining five samples were all fitted to hexagonal metallic Ru. Standard paths for the structures were created using FEFF7 software.[34] The Fourier trans-

form range was 3.5 to 11.75/Å and the fit range was 1.7 to 4.8 Å for all samples. Due to this range selection, the first four Ru-Ru standard paths and two multiscattering paths were used from the hexagonal metallic Ru structure for all fittings except for the Ru-200 sample which only used the first Ru-Ru metallic path due to a limited structure above 3 Å likely arising from disorder in the sample. Coordination number (CN) and distance ratios for all metallic samples were constrained to reflect the theoretical structure while allowing for a complete expansion or contraction. The constraints resulted in 8 degrees of freedom. Supporting information Figure S12A and Table S2 show that for sample Ru-200 the Ru-Cl path possessed a CN of 5.5 with a bond length of 2.36 Å, while for the Ru-Ru path the distance is 2.70 Å with a CN of 0.95. Again, these suggest incomplete decomposition of $RuCl_3$ into Ru nanoclusters at 200 A for 6 s. For the samples prepared at higher magnetic currents (300–600 A), the main peak appears at ca. 2.4 Å, consistent with the Ru–Ru bond in Ru foil, with a weak shoulder around 1.9 Å for the Ru-Cl bond. In addition, a small peak can be found at ca. 1.5 Å, similar to the Ru-O path of RuO_2. These observations are consistent with results from TEM and XPS measurements, where metallic Ru nanoparticles were the predominant product, and the nanoparticle surface was decorated with $RuO_x/RuCl_y$ species. Indeed, the fitting of the EXAFS data (Supporting information Figure S12B-D and Table S2) indicates that the sample structure is identical to that of the Ru foil with a Ru-Ru bond length of ca. 2.67 Å and a CN of 12. A similar structural evolution was also observed with samples prepared at 300 A but for a different heating duration (Supporting information Figures S12E-F and S13).

2.3 | Electrocatalytic activity

Significantly, the obtained Ru nanoparticles possessed a remarkable HER activity in both acidic and alkaline media. In cyclic voltammetry (CV) measurements (Supporting information Figure S14), Ru-300 can be seen to exhibit a strong adsorption and desorption of H around 0 V, consistent with the formation of Ru nanoparticles, in comparison to others in the series. Figure 4A shows the polarization curves of the samples that were prepared under different conditions in 0.5 M H_2SO_4. One can see that Ru-300 showed a much better activity than other samples with a low η_{10} of −23 mV, as compared to −53 mV for Ru-200, −81 mV for Ru-400, −113 mV for Ru-600, −117 mV for Ru-300-S, and −33 mV for Ru-300-L. Such a performance of Ru-300 actually rivals that of commercial Pt/C (η_{10} = -11 mV). The corresponding Tafel plots are depicted in Figure 4B, where Ru-300 possessed the lowest slope (26 mV/dec) among the series, indicating a
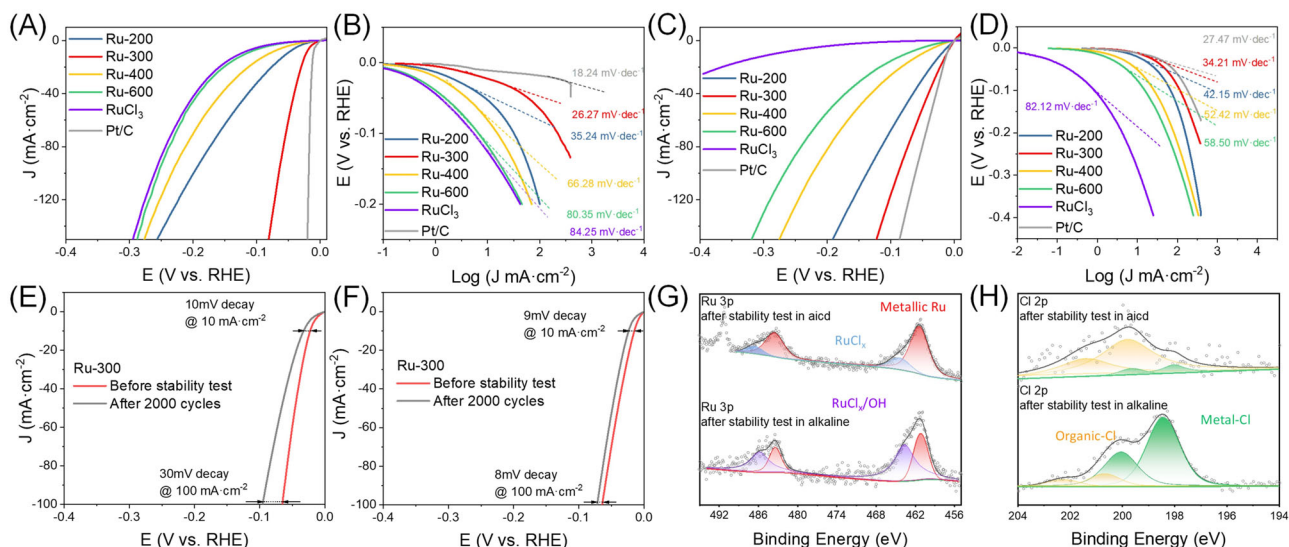
FIGURE 4 (A) Linear sweep voltammetry (LSV) curves and (B) the corresponding Tafel plots of Ru-200A, Ru-300, Ru-400, Ru-600, and RuCl$_3$ in 0.5 M H$_2$SO$_4$. (C) LSV curves of Ru-200, Ru-300, Ru-400, Ru-600, and RuCl$_3$ in 1 M KOH, and (D) stability tests of Ru-300 in (E) 0.5 M H$_2$SO$_4$ and (F) 1 M KOH. XPS spectra of the (G) Ru 2p and (H) Cl 2p electrons of Ru-300 after stability tests in acidic and alkaline media

Volmer-Tafel pathway. This pathway was also likely followed on Ru-200 and Ru-300-L, which featured a low slope of 35 and 33 mV/dec, respectively (Supporting information Figure S15). Nevertheless, the Tafel slope was markedly higher at 66 mV/dec for Ru-400, 80 mV/dec for Ru-600, and 74 mV/dec for Ru-300-S, suggesting a more sluggish Vomer–Heyrovsky pathway instead.[13,35,36]

The Ru samples also exhibited outstanding HER activity in alkaline media. Figure 4C shows the polarization curves in 1 M KOH. The η_{10} can be found to decrease drastically in the order of Ru-600 ($\eta_{10} = -78$ mV) > Ru-400 (-52 mV) > Ru-200 (-21 mV) > Ru-300 (-12 mV). Again, Ru-300 stood out as the best among the series. In the corresponding Tafel plots (Figure 4D), Ru-300 also showed a low slope of 34 mV/dec, comparable to that of Pt/C ($\eta_{10} = 12$ mV, 27 mV/dec), manifesting a Volmer–Tafel pathway.[36] Other samples exhibited relatively slower kinetics, with a Tafel slope of 42, 52, and 59 mV/dec for Ru-200, Ru-400, and Ru-600, respectively. As for Ru-300-L and Ru-300-S (Supporting information Figure S16), their η_{10} values are -28 and -64 mV, along with a Tafel slope of 59 and 37 mV/dec, respectively. Additionally, one can see that RuCl$_3$ exhibited only a minmal activity in both acidic and alkaline media, confirming that Ru nanoparticles were responsible for the HER performance. Taken together, these results indicate that Ru-300 represents the optimal catalyst within the present experimental context.

Notably, at the overpotential of -100 mV, the turnover frequency (TOF) of Ru-300 was estimated to be 0.3 s^{-1} and 0.15 s^{-1} in the acidic and alkaline media, respectively (Supporting information Figure S17). One can see that whereas the intrinsic activity in acid remains subpar as compared to

that of Pt/C, the performance in alkaline media is actually rather close (0.36 s^{-1} for Pt/C).

Ru-300 also exhibited excellent stability in both acidic and alkaline media. In accelerated LSV tests for 2000 cycles (Figure 4E and F), one can see that η_{10} in 0.5 M H$_2$SO$_4$ shifted negatively by only 10 mV and η_{100} by 30 mV, whereas in 1 M KOH, the decay of the overpotential was much smaller, with a negative shift of only 9 mV for η_{10} and 8 mV for η_{100}. This is consistent with results from XPS measurements (Figure 4G and H and Supporting information Table S1), where the Ru-Cl species remained well-defined in Ru-300 after the stability tests in both 0.5 M H$_2$SO$_4$ (0.06 at%) and in 1 M KOH (0.72 at%), though at a somewhat reduced concentration as compared to that (0.96 at%) of the as-produced sample. In contrast, no RuO$_x$ species could be resolved in XPS measurements after the stability tests (Supporting information Figure S18), suggesting that RuO$_x$ was unlikely to make substantial contributions to the HER performance.

To further highlight the unique advantages of MIH in sample preparation, we also thermally treated RuCl$_3$ in a conventional tube furnace at a comparable temperature (i.e., 300 and 500°C) under ambient conditions for 1 h. In electrochemical measurements (Supporting information Figure S19), the obtained samples behaved analogously to commercial RuO$_2$, rather than metallic Ru, and the HER activity was markedly lower than that of Ru-300. In fact, Ru-300 ranks among the best in relevant HER catalysts in the literature, but the sample preparation takes only seconds, as compared to hours for others prepared by conventional thermal procedures (Supporting information Table S3).
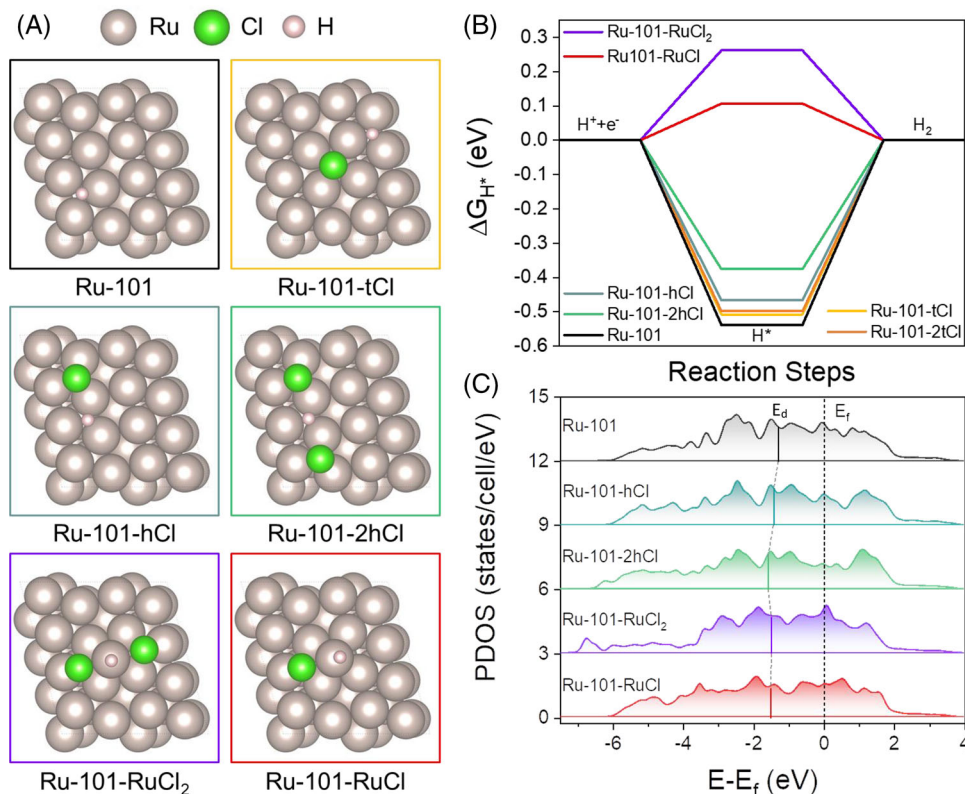
FIGURE 5 DFT studies of Ru with surface-enriched Cl. (A) Models of Ru (10-11) with various RuClₓ species. (B) Gibbs free energy of H* (ΔG_{H*}) adsorption on corresponding models in panel (A). (C) Projected density of states (PDOS) of d-electrons of Ru active sites in panel (A)

2.4 | Computational study

Based on the above experimental studies, it is likely that Ru-Cl species played an important role in the HER process. To understand the remarkable HER activity of Ru nanoparticles with surface-enriched Cl, DFT calculations were conducted to unravel the fundamental mechanism. As shown in Figure 5A, as (10-11) (i.e., (101)) is the main facet of *hcp* Ru, we used it to build the Cl-related models for H adsorption. We first tested the possibility of on-top adsorption of H on Ru-101 as the input model (Supporting information Figure S20), but it relaxed into the hollow-site adsorption (Figure 5A, black frame), confirming that the on-top adsorption is subordinate to the hollow fashion.[7] This was further evidenced by the Gibbs free energy of H adsorption (ΔG_{H*}), as shown in Figure 5B, which has been widely used as a descriptor of the HER activity. Typically, a ΔG_{H*} close to 0 eV is the ideal condition for H to adsorb and desorb. In fact, H was favorably adsorbed on the hollow site of Ru-101 with a ΔG_{H*} of −0.54 eV, indicating that desorption of H from the surface would be energetically difficult. With a Cl atom adsorbed on Ru-101 in a tetradentate fashion (Ru-101-tCl, yellow frame in Figure 5A), it was found that the ΔG_{H*} slightly shifted to −0.51 eV (Figure 5B). With two neighboring Cl adsorbates (Supporting information Figure S21), ΔG_{H*} decreased further to −0.50 eV

(Figure 5B), implying that surface-adsorbed Cl indeed could facilitate the desorption of H from the Ru-101 surface. However, the effect remains too trivial. Considering that the interaction distance between Cl and H (3.7 Å) was still too far, a closer situation was then examined, where Cl was located at the hollow site of Ru-101 (Ru-101-hCl, teal colored frame in Figure 5A), with a separation of 3.1 Å to the adsorbed H at the nearby hollow site. It was found that ΔG_{H*} decreased to −0.47 eV (Figure 5B). If another Cl was added at the hollow site of Ru-101 (Ru-101-2hCl, green frame in Figure 5A), ΔG_{H*} now diminished to −0.38 eV (Figure 5B), much improved for HER as compared to pristine Ru-101. We further considered RuClₓ species, including (RuCl₂)⁺ and (RuCl)²⁺, on the surface of the Ru slab by building models shown in Figure 5A (in purple and red frames) and Supporting information Figure S22. One can see that with such an adatom mode, the H atom could stably adsorb onto the Ru atom in an on-top fashion, and a significant change was observed with ΔG_{H*}, that is, +0.11 and +0.26 eV for Ru-101-RuCl and Ru-101-RuCl₂, respectively (Figure 5B). Taken together, these results indicate that the RuClₓ species could indeed enhance the HER activity by weakening the H adsorption.

To further investigate the mechanism of weakened H adsorption, we calculated the total density of states (DOS) and partial density of states (PDOS) of the d electrons

to understand the electronic structure of the bulk and the surface atoms. One can see from Supporting information Figure S23 that the total DOS of several models with adsorbed Cl or $RuCl_x$ species all have similar profiles, meaning similar bulk electronic properties near the Fermi level, in agreement with the lack of significant difference among the Ru K-edge adsorption edges in XANES study (Figure 3). Further analysis of PDOS of the Ru active sites (Figure 5C) showed an apparent change of the Ru d electrons, especially the d band centers (E_d). One can see that in comparison with the surface Ru of Ru-101, where E_d is located at −1.33 eV, with the adsorption of even only one Cl, the neighboring Ru on Ru-101-hCl shifts negatively to −1.44 eV; and for Ru-101-2hCl (with the adsorption of two Cl's), the E_d downshifts further to −1.59 eV. Meanwhile, from Supporting information Figure S24, it can be seen that the E_d of Ru atoms without direct coordination with Cl also shifted slightly to −1.40 eV, signifying that adsorption of Cl atoms rendered a strong impact on the local electronic structure. Furthermore, both Ru-101-RuCl and Ru-101-RuCl$_2$ can be seen to exhibit a downshift of E_d to −1.52 and −1.50 eV, respectively (Figure 5C), significantly different from the pristine Ru-101.

Further insights into the interactions between Ru nanoparticles and $RuCl_x$ or Cl ligands were obtained by Bader charge analysis, as shown in Supporting information Figure S25 and S26. A *hcp* Ru (10–11) slab was built with surface adsorption of Cl^-, $(RuCl)^{2+}$, and $(RuCl_2)^+$ species to represent the incomplete decomposition of $RuCl_3$. It should be noted that $RuCl_3$ would spontaneously decompose into Cl^- and Ru atoms on the Ru slab (Supporting information Figure S27). Significantly, one can see that efficient charge transfer occurred from the Ru slab to these Cl species (Supporting information Figure S26). For one adsorbed Cl^-, it could withdraw 0.40 electron from the Ru slab, whereas 0.49 and 0.81 electrons from the Ru slab to $(RuCl)^{2+}$ and $(RuCl_2)^+$, respectively.[37–40] It is, therefore, likely that such interfacial charge transfer was responsible for the downshift of E_d and weakened adsorption of H on the Ru nanoparticle surface, leading to enhanced HER activity, as observed experimentally.[38,41,42]

3 | CONCLUSIONS

In summary, MIH was exploited for the ultrafast and green preparation of Ru nanoparticles supported on carbon paper. The samples could be prepared within seconds, and the rapid synthesis led to the formation of metal-Cl species on the Ru nanoparticle surface. With this unique structural feature, all the samples exhibited apparent electrocatalytic activity toward HER in both acidic and alkaline media, and the best sample, Ru-300, needed an over-

potential of only −23 and −12 mV to reach 10 mA/cm^2, respectively, rivaling the commercial Pt/C benchmark, along with excellent stability. Results from DFT calculations showed that the surface Cl species induced apparent electron transfer from the Ru nanoparticles, leading to a downshift of the Ru E_d, and, hence weakened H adsorption, a unique feature for enhanced HER activity, as observed experimentally. Results from this study highlight the unique significance of MIH in the structural engineering of metal nanoparticles by heteroanion functionalization for enhancement of their electrocatalytic performance.

4 | EXPERIMENTAL SECTION

4.1 | Chemicals

Ruthenium(III) chloride hydrate ($RuCl_3 \cdot xH_2O$, 35–40%, ACROS Organics), acetone (Fisher Chemicals), carbon paper (TGP-H-90, Toray), ruthenium(IV) oxide (RuO_2, 99.5%, anhydrous, ACROS Organics), and Pt/C (20 wt.%, Alfa Aesar) were used as received. Water was purified with a Barnstead Nanopure Water System (18.2 MΩ cm).

4.2 | Sample synthesis

Carbon paper was thermally treated in a Muffle furnace at 500°C in ambient for 1 h to increase surface wettability, cut into 1×2 cm^2 pieces, and rinsed with acetone several times. $RuCl_3$ was dissolved into acetone to form a solution at a concentration of 20 mg/mL, 100 μL of which was then dropcast onto the carbon paper. After drying in air for 30 min, the carbon paper was wrapped in graphite paper (0.01 mm thick) before being sandwiched between two iron sheets (2.5 cm × 2.5 cm × 0.01 mm) to prevent direct contact of the samples with the iron sheets. The assembly was then placed in the center of a four-turn induction coil with a diameter of 5 cm, and MIH was carried out at a controlled current (X = 200–600 A) for a select heating time (Y = 3–12 s), when the sample was dropped into an ethanol-dry ice solution (−78°C) placed underneath the induction coil for rapid quenching (caution: the ethanol must be fully cooled down by dry ice, or it will catch fire). Control samples were also prepared in a tube furnace at a comparable temperature (i.e., 300 and 500°C) for 1 h under ambient conditions.

4.3 | Characterizations

TEM images were acquired with a Tecni G2 operated at 200 kV. XPS measurements were carried out with a

Thermo Fisher K-alpha system, where the binding energy was calibrated against the C 1s binding energy. Raman measurements were conducted using a Horiba Jobin Yvon LabRAM ARAMIS automated scanning confocal Raman microscope under 532 nm excitation. XAS measurements were carried out at 10 K on beamline 4-1 of the Stanford Synchrotron Radiation Lightsource using an Oxford liquid helium cryostat.

4.4 | Electrochemistry

Electrochemical measurements were carried out with a CHI 700E electrochemical workstation in a three-electrode configuration. The obtained carbon paper was fixed onto a graphite electrode holder, with an exposed surface area of 0.25 cm^2. A graphite rod was used as the counter electrode and a Ag/AgCl in saturated KCl as the reference electrode. The reference electrode was calibrated against a reversible hydrogen electrode (RHE) and all potentials in the present study were referenced to this RHE. To load Pt/C onto the carbon paper, 1 mg of Pt/C (20%) was dispersed under sonication in 190 μL of isopropanol solution and 10 μL of 100% Nafion solution; and 125 μL of the dispersion was dropcast onto part of the carbon paper (with an area of 0.25 cm^2). RuO$_2$ was deposited onto the carbon paper in the same fashion at the same metal loading.

4.5 | Theoretical study

First-principle computations were performed using Quantum ESPRESSO, an open-source plane-wave code.[43] A 4 × 4-unit cell with 48 atoms was used to build a hexagonal Ru (10-11) slab supercell, where periodic image interactions were removed by setting a vacuum of 15 Å. Ru atoms of the bottom layer have been fixed during all relax calculations. A cut-off of 50 and 500 Ry for kinetics and charge density was chosen with the GBRV ultrasoft pseudopotential.[44] The total energy of the Monkhorst-Pack 4 × 4 × 1 K-point grid in the supercell was calculated at the convergence level of 1 meV per atom. The smearing parameter was set at 0.01 Ry in the Marzari–Vanderbilt smearing for all calculations.[45] For geometric relaxation, the convergence was 10^{-8} Ry of the electronic energy and 10^{-4} Au for the total force. Density functional perturbation theory was employed to calculate the phonon frequency as an input for entropy and zero-point energy.[46]

CONFLICT OF INTERESTS
The authors declare no conflict of interest.

DATA AVAILABILITY STATEMENT
All data supporting the findings of this study are available within the article and the Supplementary Information file. All data are available upon request from the corresponding author.

ORCID
*Shaowei Chen* https://orcid.org/0000-0002-3668-8551

REFERENCES
1. Turner JA. Sustainable hydrogen production. *Science*. 2004;305(5686):972-974.
2. Wang YX, Su HY, He YH, et al. Advanced electrocatalysts with single-metal-atom active sites. *Chem Rev*. 2020;120(21):12217-12314.
3. Song W, Li M, Wang C, Lu X. Electronic modulation and interface engineering of electrospun nanomaterials-based electrocatalysts toward water splitting. *Carbon Energy*. 2021;3(1):101-128.
4. Mitchell WJ, Xie J, Jachimowski TA, Weinberg WH. Carbon-monoxide hydrogenation on the Ru(001) surface at low-temperature using gas-phase atomic-hydrogen - spectroscopic evidence for the carbonyl insertion mechanism on a transition-metal surface. *J Am Chem Soc*. 1995;117(9):2606-2617.
5. Yang YJ, Yu YH, Li J, et al. Engineering ruthenium-based electrocatalysts for effective hydrogen evolution reaction. *Nano-Micro Lett*. 2021;13(1):160.
6. Skulason E, Tripkovic V, Bjorketun ME, et al. Modeling the electrochemical hydrogen oxidation and evolution reactions on the basis of density functional theory calculations (vol 114, pg 18182, 2010). *J Phys Chem C*. 2010;114(50):22374-22374.
7. Chen H, Ai X, Liu W, et al. Promoting subordinate, efficient ruthenium sites with interstitial silicon for pt-like electrocatalytic activity. *Angew Chem Int Edit*. 2019;58(33):11409-11413.

8. Yao YG, Huang ZN, Xie PF, et al. Carbothermal shock synthesis of high-entropy-alloy nanoparticles. *Science.* 2018;359(6383):1489-1494.

9. Seh ZW, Kibsgaard J, Dickens CF, Chorkendorff IB, Norskov JK, Jaramillo TF. Combining theory and experiment in electrocatalysis: insights into materials design. *Science.* 2017;355(6321):aad4998.

10. Ding Y, Cao K-W, He J-W, et al. Nitrogen-doped graphene aerogel-supported ruthenium nanocrystals for pH-universal hydrogen evolution reaction. *Chinese Journal of Catalysis.* 2022;43(6):1535-1543.

11. Peng Y, Pan WZ, Wang N, Lu JE, Chen SW. Ruthenium ion-complexed graphitic carbon nitride nanosheets supported on reduced graphene oxide as high-performance catalysts for electrochemical hydrogen evolution. *Chemsuschem.* 2018;11(1):130-136.

12. Peng Y, Lu BZ, Chen LM, et al. Hydrogen evolution reaction catalyzed by ruthenium ion-complexed graphitic carbon nitride nanosheets. *J Mater Chem A.* 2017;5(34):18261-18269.

13. Lu BZ, Guo L, Wu F, et al. Ruthenium atomically dispersed in carbon outperforms platinum toward hydrogen evolution in alkaline media. *Nat Commun.* 2019;10(1):631.

14. Cai C, Liu K, Zhu YM, et al. Optimizing hydrogen binding on ru sites with RuCo alloy nanosheets for efficient alkaline hydrogen evolution. *Angew Chem Int Edit.* 2022;61(4):e202113664.

15. Chen D, Liu TT, Wang PY, et al. Ionothermal route to phase-pure RuB2 catalysts for efficient oxygen evolution and water splitting in acidic media. *Acs Energy Lett.* 2020;5(9):2909-2915.

16. Qiao YY, Yuan PF, Pao CW, et al. Boron-rich environment boosting ruthenium boride on B, N doped carbon outperforms platinum for hydrogen evolution reaction in a universal pH range. *Nano Energy.* 2020;75:104881.

17. Wang J, Han LL, Huang BL, Shao Q, Xin HLL, Huang XQ. Amorphization activated ruthenium-tellurium nanorods for efficient water splitting. *Nat Commun.* 2019;10(1):5692.

18. Zhou F, Sa RJ, Zhang X, Zhang S, Wen ZH, Wang RH. Robust ruthenium diphosphide nanoparticles for pH-universal hydrogen evolution reaction with platinum-like activity. *Appl Catal B-Environ.* 2020;274:119092.

19. Zhu SQ, Qin XP, Xiao F, et al. The role of ruthenium in improving the kinetics of hydrogen oxidation and evolution reactions of platinum. *Nat Catal.* 2021;4(8):711-718.

20. Zhao YM, Wang XW, Cheng GZ, Luo W. Phosphorus-induced activation of ruthenium for boosting hydrogen oxidation and evolution electrocatalysis. *Acs Catal.* 2020;10(20):11751-11757.

21. Morgan DJ. Resolving ruthenium: xPS studies of common ruthenium materials. *Surf Interface Anal.* 2015;47(11):1072-1079.

22. Bock C, Paquet C, Couillard M, Botton GA, MacDougall BR. Size-selected synthesis of PtRu nano-catalysts: reaction and size control mechanism. *J Am Chem Soc.* 2004;126(25):8028-8037.

23. Ren XM, Guo M, Li H, et al. Microenvironment engineering of ruthenium nanoparticles incorporated into silica nanoreactors for enhanced hydrogenations. *Angew Chem Int Edit.* 2019;58(41):14483-14488.

24. Ruppert AM, Jedrzejczyk M, Sneka-Platek O, et al. Ru catalysts for levulinic acid hydrogenation with formic acid as a hydrogen source. *Green Chem.* 2016;18(7):2014-2028.

25. Man BC, Zhang HY, Zhang CM, et al. Effect of Ru/Cl ratio on the reaction of acetylene hydrochlorination. *New J Chem.* 2017;41(23):14675-14682.

26. Giulimondi V, Kaiser SK, Agrachev M, et al. Redispersion strategy for high-loading carbon-supported metal catalysts with controlled nuclearity. *J Mater Chem A.* 2021(10):5953-5961.

27. Chen SQ, Ling LL, Zhang S, et al. Sustainable in situ carbothermal reduction route to biochar stabilized Ru-Cu nanoalloys from lignocellulosic biomass as a highly efficient and durable catalyst. *Adv Sustain Syst.* 2017;1(12):1700102.

28. Park K, Padmanaban S, Kim SH, Jung KD, Yoon S. NNN pincer-functionalized porous organic polymer supported Ru(III) as a heterogeneous catalyst for levulinic acid hydrogenation to gamma-valerolactone. *Chemcatchem.* 2021;13(2):695-703.

29. Lebedeva A, Albuquerque BL, Domingos JB, et al. Ruthenium trichloride catalyst in water: Ru colloids versus ru dimer characterization investigations. *Inorg Chem.* 2019;58(7):4141-4151.

30. Zhao HZ, Lei M, Yang X, Jian JK, Chen XL. Route to GaN and VN assisted by carbothermal reduction process. *J Am Chem Soc.* 2005;127(45):15722-15723.

31. Lee JH, Choi Y, Do SH, Kim BH, Seong MJ, Choi KY. Multiple spin-orbit excitons in alpha-RuCl3 from bulk to atomically thin layers. *Npj Quantum Mater.* 2021;6(1):43.

32. Li GM, Chen XB, Gang Y, et al. Raman spectroscopy evidence for dimerization and Mott collapse in alpha-RuCl3 under pressures. *Phys Rev Mater.* 2019;3(2):023601.

33. Mai TT, McCreary A, Lampen-Kelley P, et al. Polarization-resolved Raman spectroscopy of alpha-RuCl3 and evidence of room-temperature two-dimensional magnetic scattering. *Phys Rev B.* 2019;100(13):134419.

34. Ankudinov AL, Rehr JJ. Relativistic calculations of spin-dependent x-ray-absorption spectra. *Phys Rev B.* 1997;56(4):R1712-R1715.

35. Dechialvo MRG, Chialvo AC. Hydrogen evolution reaction - analysis of the volmer-heyrovsky-tafel mechanism with a generalized adsorption model. *J Electroanal Chem.* 1994;372(1-2):209-223.

36. Bhardwaj M, Balasubramaniam R. Uncoupled non-linear equations method for determining kinetic parameters in case of hydrogen evolution reaction following Volmer-Heyrovsky–Tafel mechanism and Volmer–Heyrovsky mechanism. *Int J Hydrogen Energ.* 2008;33(9):2178-2188.

37. Ciganda R, Li N, Deraedt C, et al. Gold nanoparticles as electron reservoir redox catalysts for 4-nitrophenol reduction: a strong stereoelectronic ligand influence. *Chem Commun.* 2014;50(70):10126-10129.

38. Peng Y, Liu QM, Lu BZ, et al. Organically capped iridium nanoparticles as high-performance bifunctional electrocatalysts for full water splitting in both acidic and alkaline media: impacts of metal-ligand interfacial interactions. *Acs Catal.* 2021;11(3):1179-1188.

39. Kang XW, Zuckerman NB, Konopelski JP, Chen SW. Alkyne-stabilized ruthenium nanoparticles: manipulation of intraparticle charge delocalization by nanoparticle charge states. *Angew Chem Int Edit.* 2010;49(49):9496-9499.

40. Hu PG, Chen LM, Kang XW, Chen SW. Surface functionalization of metal nanoparticles by conjugated metal-ligand interfacial bonds: impacts on intraparticle charge transfer. *Accounts Chem Res.* 2016;49(10):2251-2260.

41. Xin HL, Vojvodic A, Voss J, Norskov JK, Abild-Pedersen F. Effects of d-band shape on the surface reactivity of transition-metal alloys. *Phys Rev B.* 2014;89(11):115114.

42. Kitchin JR, Norskov JK, Barteau MA, Chen JG. Role of strain and ligand effects in the modification of the electronic and chemical properties of bimetallic surfaces. *Phys Rev Lett.* 2004;93(15):156801.

43. Giannozzi P, Baroni S, Bonini N, et al. QUANTUM ESPRESSO: a modular and open-source software project for quantum simulations of materials. *J Phys-Condens Mat.* 2009;21(39):395502.

44. Garrity KF, Bennett JW, Rabe KM, Vanderbilt D. Pseudopotentials for high-throughput DFT calculations. *Comp Mater Sci.* 2014;81:446-452.

45. Marzari N, Vanderbilt D, De Vita A, Payne MC. Thermal contraction and disordering of the Al(110) surface. *Phys Rev Lett.* 1999;82(16):3296-3299.

46. Baroni S, de Gironcoli S, Dal Corso A, Giannozzi P. Phonons and related crystal properties from density-functional perturbation theory. *Rev Mod Phys.* 2001;73(2):515-562.

AUTHOR BIOGRAPHIES
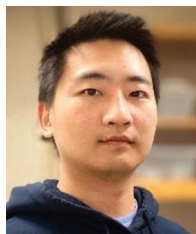
Qiming Liu received his BE degree in Materials Chemistry in 2018 from Central South University, China, and joined Professor Shaowei Chen's group at the University of California at Santa Cruz (UCSC) to pursue a PhD degree in chemistry. His current research interests concentrate on single atom catalysts toward energy conversion, ligand functionalization of nanoparticles, and ultrafast synthesis of electrocatalysts.

Dr. Bingzhang Lu received his BS degree of Chemistry in 2015 from the University of Science and Technology of China (USTC) and a PhD degree from UCSC in 2020 under the supervision of Professor Shaowei Chen. He is currently working as a postdoctoral scholar in Northwestern University with Professor Linsey Seitz. His research interest includes design and synthesis of metal oxide and carbon materials toward electrocatalysis, X-ray technique-based material characterization, and first principal calculations for electrochemical mechanistic studies.

Shaowei Chen received his BS degree in chemistry from USTC in 1991, and his MS and PhD degrees from Cornell University in 1993 and 1996, respectively. Following a postdoctoral appointment at the University of North Carolina at Chapel Hill, he started his independent career in Southern Illinois University in 1998. In 2004, he moved to UCSC. He is currently a Professor of chemistry and the faculty director of the UCSC COSMOS program. His research interests are primarily focused on high-performance catalysts for electrochemical energy conversion and storage, impacts of metal–ligand interfacial bonding interactions on nanoparticle charge-transfer dynamics, Janus nanoparticles by interfacial engineering, and antimicrobial activity of functional nanomaterials.

SUPPORTING INFORMATION

Additional supporting information can be found online in the Supporting Information section at the end of this article.